An efficient method for calculating spherical-wave reflection coefficients

Charles P. Ursenbach and Arnim B. Haase

ABSTRACT

A method is presented for efficiently calculating the spherical-wave generalization of the Zoeppritz PP reflection coefficients. The main restriction is in choosing a particular form of wavelet that allows for analytic integration over frequencies. This, combined with calculating only one time point instead of the entire time trace, results in calculations sufficiently rapid to be carried out interactively on the computer. The method is implemented both in MATLAB and as an interactive Java applet, and results are shown for an AVO Class I model. It is also shown that the calculation of spherical-wave reflection coefficients can, in practice, be cast as a weighted integral of a relatively small set of plane-wave reflection coefficients, which may allow one to achieve still more efficient calculations.

INTRODUCTION

This paper is concerned with the calculation of reflection coefficients for spherical waves in a two-layer elastic model, illustrated in the diagram below:

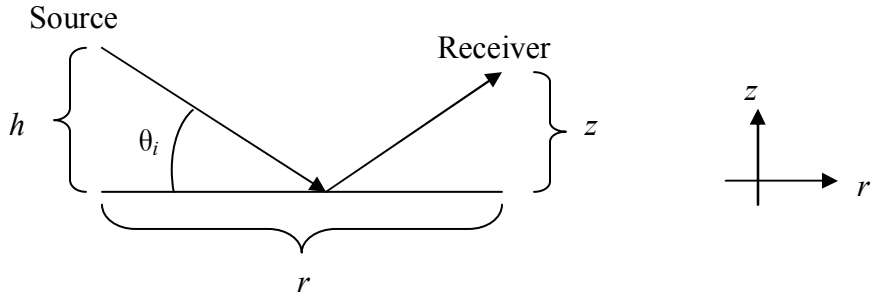

The plane-wave reflection coefficient for this system is the well-known Zoeppritz expression, $R_{PP}(p;\alpha_1,\beta_1,\rho_1;\alpha_2,\beta_2,\rho_2)$, where p is a ray parameter (the horizontal P-wave slowness), α, β, and ρ are P-wave velocity, S-wave velocity, and density, and subscripts 1 and 2 refer to upper and lower media. The generalized reflection coefficient associated with spherical waves, which includes contributions from both reflected and head waves, is given as an integral over $R_{PP}(p)$. The fundamental theory is well-established. It is given in detail, for example, by Aki and Richards (1980). They express the frequency-dependent potential as a weighted integral over all ray parameters of cylindrical waves times plane-wave reflection coefficients. In analogy with their Eq. (6.30) for free surface reflections, we can write the pertinent expression for the solid-solid interface as

$$\phi(\omega) = Ai\omega \exp(-i\omega t)\int_0^\infty R_{\mathrm{PP}}\left(p;\alpha_1,\beta_1,\rho_1,\alpha_2,\beta_2,\rho_2\right)\frac{p}{\xi}J_0(\omega pr)\exp[i\omega\xi(z+h)]dp \quad (1)$$

Here A is a scaling factor, ω is the frequency, t is time, ξ is the vertical P-wave slowness in the upper layer, J_0 is the zero-order Bessel function, r is the horizontal receiver coordinate (with the horizontal source position equal to zero), h is the vertical source position, and z is the vertical receiver coordinate.

The displacement is obtained by applying a gradient in the receiver position to the above potential. Weighting by the wavelet and applying an inverse Fourier transform yields the time trace observed at the receiver. AVO information can be extracted from maxima in the trace envelope. The above method was implemented in numerical calculations by Haase (2002, 2003, 2004a). He has also carried out this procedure for converted waves (Haase, 2004a) and with viscoelasticity (Haase, 2004b).

The above calculations are time-consuming, and most work prior to Haase has employed monochromatic wavelets (e.g., Macdonald et al., 1987). Even then it has been tempting to look for approximations. For instance, Krail and Brysk (1983) developed an approximation to Eq. (1) consisting of a series expansion in $(1/kr)$, where k is the wavenumber and r is the radius. In addition R_{PP} and J_0 are replaced by Taylor series expansions. Furlong et al. (1994) developed a somewhat different approximation that consists of assuming that the reflected and transmitted waves are spherical (or dipolar for converted waves). The reflection coefficients are then obtained by matching boundary conditions across the interface, analogous to the Zoeppritz coefficient derivation.

The effect of approximations in these earlier works is not well understood, particularly in the vicinity of critical points. Furthermore, when methods assume a monochromatic wavelet, it becomes difficult to assess their implications for practical AVO inversion. Haase's numerical evaluation of exact expressions provides benchmark results for realistic seismic wavelets and confirms that spherical-wave reflections differ significantly from plane waves near critical points. This is important, for instance, when using AVO inversion to extract density information for Class I interfaces. Still, the exact calculations may be too time-consuming to apply easily to AVO problems. The method proposed in this paper leaves the theoretical framework intact, and imposes restrictions only on the form of the wavelet. Results below indicate that this approximation leaves the general behavior of the reflection coefficient unchanged.

THEORETICAL DEVELOPMENT

Integration over ω

Beginning with Eq. (1), let us define an integrated potential as

$$\Phi(t) = \int_{-\infty}^{\infty} f(\omega)\phi(\omega)d\omega. \quad (2)$$

In this expression $f(\omega)$ is the wavelet and we will define it to be of the following form:

$$f(\omega) \propto \omega^n \exp(-|s\omega|), \quad n = 0,1,2,..., \quad 0 < s < \infty. \tag{3}$$

We can interchange the order of p and ω integrations[1], as shown here:

$$\begin{aligned}\Phi(t) &= \int_{-\infty}^{\infty} \omega^n \exp(-|s\omega|)\left[Ai\omega \exp(-i\omega t)\int_0^{\infty} R_{\mathrm{PP}}(p)\frac{p}{\xi} J_0(\omega pr)\exp[i\omega\xi(z+h)]dp \right] d\omega \\ &= Ai\int_0^{\infty} R_{\mathrm{PP}}(p)\left[\int_{-\infty}^{\infty} \omega^{n+1} J_0(\omega pr)\exp(-|s\omega| - i(t-\xi[z+h])\omega) d\omega \right]\frac{p}{\xi}dp \\ &\equiv Ai\int_0^{\infty} R_{\mathrm{PP}}(p)[I_R(p)]\frac{p}{\xi}dp.\end{aligned} \tag{4}$$

In the last step we define $I_R(p)$ as a result of integration over ω. It is advantageous to change the lower bound of the ω-integration to zero. This will lead us directly to the analytic or complex trace, whose real part is proportional to the original integral. We shall require the analytic trace later, so it is convenient to obtain it in this way. Effectively we replace $I_R(p)$ in Eq. (4) with $I(p) = ½\ [I_R(p) + i\ I_I(p)]$, where $I_R(p)$ and $I_I(p)$ are real functions. Changing the lower bound to zero also gives the integral the form of a Laplace transform, and an analytic solution is available (Erdelyi, 1954):

$$\begin{aligned} I(p) &= \frac{(n+1)!}{\tau^{n+2}} P_{n+1}\left(\frac{T}{\tau}\right) \\ T &= s + i(t - \xi[z+h]) \quad , \\ \tau &= \sqrt{T^2 + p^2 r^2} \end{aligned} \tag{5}$$

where $P_n(x)$ is a Legendre polynomial.

Calculation of the gradient

Next one takes the gradient with respect to receiver position so that the final reflection coefficient will be for displacements. If we assume that displacement is in the direction of propagation of the reflected wave, then we can begin by substituting $z = R\cos(\theta_i) - h$ and $r = R\sin(\theta_i)$, which effectively defines θ_i as the angle of incidence and R as the distance traveled by the wave. The desired derivative is then obtained by taking a simple derivative with respect to R. This yields

[1] Bortfeld (1962) justifies changing the order of integration for this integral. He develops a method in which a sinc function wavelet is employed for the integration over frequency, and the actual seismic wavelet is introduced at the end of the procedure by convolution. His method is therefore more general than the present approach, but also more computationally intensive.

$$\frac{\partial I}{\partial R} = -\frac{(n+2)!}{\tau^{n+3}} P_{n+1}\left(\frac{T}{\tau}\right)\frac{\partial \tau}{\partial R} + \frac{(n+1)!}{\tau^{n+2}}\left[P_n\left(\frac{T}{\tau}\right) - \frac{T}{\tau}P_{n+1}\left(\frac{T}{\tau}\right)\right]\frac{\partial}{\partial R}\left(\frac{T}{\tau}\right),$$
$$\frac{\partial T}{\partial R} = -i\xi\cos\theta_i, \qquad (6)$$
$$\frac{\partial \tau}{\partial R} = \frac{-i\xi T\cos\theta_i + Rp^2\sin^2\theta_i}{\tau}.$$

We should bear in mind that the assumption regarding the direction of displacement of the reflected wave may not be valid in the vicinity of the critical point, where it cannot be distinguished from the head wave. However, the directional difference in this region is small, and results shown below suggest that it is a reasonable assumption.

Simplifications

Eq. (6) is a function of time, t. Let us assume that the signal of interest will arrive at the receiver at time R/α. (The discussion regarding the direction-of-displacement assumption probably applies here as well.) Let us set $t = R/\alpha$ (this can only be done *after* applying the gradient), and let us further set $p = \sin\theta / \alpha$ and $\xi = \cos\theta / \alpha$. It will also be convenient to define $S \equiv s\alpha/R$, as a quantity indicating the importance of spherical effects. These steps allow us to produce reasonably simple explicit expressions for particular values of n, which will be suitable for computer programming. In particular, the quantities T and τ which appear on the right-hand sides in Eq. (6) can be written as

$$T = (R/\alpha)[S + i(1-\cos\theta\cos\theta_i)],$$
$$\tau = \sqrt{T^2 + (R/\alpha)^2\sin^2\theta\sin^2\theta_i}. \qquad (7)$$

We note that for a wavelet of the form of Eq. (3), the maximum amplitude, ω_{max}, occurs at n/s. For a monochromatic wavelet, the quantity controlling the size of spherical effects is $\alpha/(R\omega)$, which in our notation is S/n for ω_{max} ($n \neq 0$). It is therefore reasonable that the quantity S arises naturally in this theory.

Changing the variable of integration

Collecting the above results together, we can formally write our spherical-wave reflection displacement amplitude as

$$R_{PP}^{sph}(\theta_i;\alpha_1,\beta_1,\rho_1,\alpha_2,\beta_2,\rho_2) = Ai\int_0^\infty R_{PP}(p;\alpha_1,\beta_1,\rho_1,\alpha_2,\beta_2,\rho_2)\frac{p}{\xi}\frac{\partial I}{\partial R}dp. \qquad (8)$$

For the numerical implementation to follow, a change of variables will be used to replace p with $\cos\theta$ as the integration variable, where $\cos\theta = \sqrt{(1-\alpha^2p^2)}$. From the relation $p^2 + \xi^2 = 1/\alpha^2$ we derive the differential relation $(p/\xi)dp = -d\xi = -d(\cos\theta)/\alpha$. Also, let us divide

the integration range into two parts: $\int_0^\infty \cdots dp = \left[\int_0^{1/\alpha} + \int_{1/\alpha}^\infty\right] \cdots dp$. In changing the variable of integration to cosθ we express this as $\left[\int_1^0 + \int_{i0}^{i\infty}\right] \cdots d(\cos\theta)$. We then rewrite Eq. (8) as

$$R_{\mathrm{PP}}^{\mathrm{sph}}(\theta_i) = A\left[\int_0^1 - \int_{i0}^{i\infty}\right] R_{\mathrm{PP}}(\theta)\left(\frac{i}{\alpha}\frac{\partial I}{\partial R}\right) d(\cos\theta). \tag{9}$$

We see from Eq. (9) that $(i/\alpha)(\partial I / \partial R)$ acts as a weighting function in cosθ to transform $R_{\mathrm{PP}}(\theta)$ to $R_{\mathrm{PP}}^{\mathrm{sph}}(\theta_i)$.

Normalization

Spherical waves decrease in amplitude with distance traveled, while planes waves do not. This complicates comparison of reflection coefficients. It is desirable to remove the spherical divergence and near-field effects and to thus isolate the effect on amplitude of reflection alone. One simple approach is to normalize the spherical-wave result by the result that would be obtained if the reflection coefficient were set to unity. Setting $R_{\mathrm{PP}} = 1$ in Eq. (1) allows the integral over p (the Sommerfeld integral) to be done analytically, recovering the simpler potential of the spherical wave,

$$\frac{A}{R}\exp\left[-i\omega\left(t - \frac{R}{\alpha}\right)\right]. \tag{10}$$

Taking the derivative with respect to R, setting $t = R/\alpha$, and then weighting by the wavelet and integrating over frequency yields the analytic trace result

$$A\left[-\frac{n!}{s^{n+1}R^2} + i\frac{(n+1)!}{\alpha s^{n+2}R}\right]. \tag{11}$$

Dividing Eq. (9) by Eq. (11) gives a normalized reflection coefficient suitable for comparison with the plane wave result. If Eq. (11) is incorporated earlier, by dividing it into the weighting function, $\frac{i}{\alpha}\frac{\partial I}{\partial R}$, then a normalized weighting function results, the real part integrating to one, and the imaginary part to zero. We will denote this

$$W_n = \frac{\dfrac{i}{\alpha}\dfrac{\partial I}{\partial R}}{-\dfrac{n!}{s^{n+1}R^2} + i\dfrac{(n+1)!}{\alpha s^{n+2}R}} \tag{12}$$

with

$$\left[\int_0^1 - \int_{i0}^{i\infty}\right] W_n(\theta, \theta_i, S)\, d(\cos\theta) = 1 + 0i. \tag{13}$$

We can then write the ratio of Eq. (9) and Eq. (11) formally as

$$\text{normalized } R_{\text{PP}}^{\text{sph}}(\theta_i) = \left[\int_0^1 - \int_{i0}^{i\infty}\right] R_{\text{PP}}(\theta) W_n(\theta, \theta_i, S)\, d(\cos\theta). \tag{14}$$

The $n = 0$ case

This is the simplest case, but $\exp(-|s\omega|)$ is not a very realistic wavelet from a seismic point of view. However we include it as it is instructive on a few points. We can evaluate the above expressions to obtain the normalized weighting function,

$$\begin{aligned}
W_0(\theta, \theta_i, S) &= \frac{A + iBS}{\left\{[\cos(\theta) - \cos(\theta_i)]^2 - 2iS[1 - \cos(\theta)\cos(\theta_i)] - S^2\right\}^{5/2}} \frac{S^2}{1 + iS}, \\
A &= 2\cos(\theta)\cos(\theta_i)[\cos(\theta) - \cos(\theta_i)]^2 + 3\sin^2(\theta)\sin^2(\theta_i) \\
&\quad + 2S^2[2 - 3\cos(\theta)\cos(\theta_i)], \\
B &= 2[\cos(\theta) - \cos(\theta_i)]^2 - 4\cos(\theta)\cos(\theta_i)[1 - \cos(\theta)\cos(\theta_i)] - 2S^2.
\end{aligned} \tag{15}$$

This function depends explicitly only on θ, θ_i, and $S = s\alpha/R$. The sin terms appear as squares, so all θ and θ_i dependence can be expressed in terms of $\cos\theta$ and $\cos\theta_i$. This is obviously convenient for integration over $\cos\theta$. Quantities (other than θ_i) which affect the magnitude of spherical effects are combined in the dimensionless quantity S. Spherical effects increase with increasing velocity in the overburden ($\alpha\uparrow$), decreasing distance traveled by the wavelet ($R\downarrow$), and increasing width of the wavelet ($s\uparrow$). Thus increasing S corresponds to increasing spherical effects.

In the limit of *decreasing* S the envelope of W_0 yields

$$\lim_{S\to 0}|W_0| = \left|\frac{2\cos(\theta)\cos(\theta_i)\left[\cos(\theta) - \cos(\theta_i)\right]^2 + 3\sin^2(\theta)\sin^2(\theta_i)}{\left|\cos(\theta) - \cos(\theta_i)\right|^5}\right| \lim_{S\to 0} S^2. \tag{16}$$

This will vanish for all values of θ except for $\theta = \theta_i$, at which point it may diverge. The real and imaginary components of W_0 are bounded by the envelope. Thus, because the real part is normalized to 1, it will act as a delta function in this limit, reducing the spherical-wave reflection coefficient down to the plane wave Zoeppritz coefficient.

The corresponding expressions for $n > 0$ are more complicated, but possess the same properties as described here for $n = 0$. They have been obtained using a symbolic mathematics program (MAPLE) and implemented for numerical computation (MATLAB and Java). We present results below for $n = 4$, as this can be used to approximately model the frequency content of a seismic wavelet.

APPLICATION

Description of model

We construct an application intended for comparison with results from Haase (2004a). Consider a two-layer model with earth parameters specified in Table I. This constitutes a Class I AVO system, and it possesses a critical point at ~ 43°.

Table I. Earth parameters for a two-layer, Class I AVO model.

	Upper Layer	Lower Layer
V_P (m/s)	2000	2933.33
V_S (m/s)	879.88	1882.29
ρ (kg/m3)	2400	2000

Haase (2004a) employs an Ormsby wavelet, 5/15-80/100 Hz. We have approximated this by a wavelet of the form of Eq. (3), where $n = 4$, and $s = (0.173 \text{ s})/(2\pi)$. The two wavelets are displayed together in Figure 1 below. Clearly there is no sort of quantitative matching, and one can only hope to reproduce the general frequency range of a given wavelet by a function of the form of Eq. (3). In this case we have attempted primarily to reproduce the lower frequencies, as these are presumably more important in reproducing spherical-wave effects.

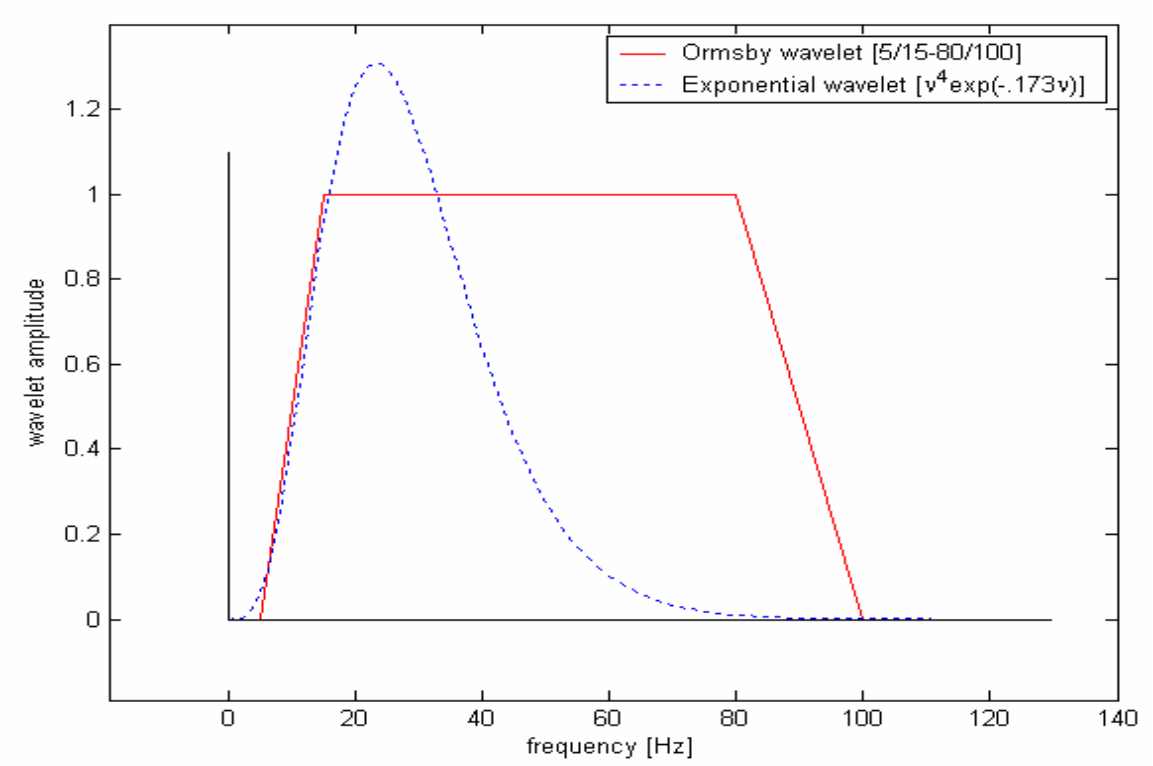

FIG. 1. Comparison of 5/15-80/100 Ormsby wavelet (solid red line) with a wavelet of the form of Eq. (3) with n = 4, s = (.173 s)/(2π) (dashed blue line). Emphasis has been given to matching the lower frequencies.

Following Haase we also employ a depth of $z = h$ = 500m, and an overburden P-wave velocity of α = 2000 m/s (see Table I above). This, together with s, specifies S, which completely determines the deviation from plane wave behavior for this wavelet.

Details of implementation

To calculate the normalized spherical reflection coefficients we must implement Eq. (14) as an algorithm. The integrand is a product of two factors:

- The plane wave reflection coefficient, R_{PP}, which depends on velocities and densities of the two earth layers, and on the integration variable;
- The normalized weighting function, W_n, which depends on the angle of incidence, θ_i, on the wavelet parameters, n and S, and on the integration variable.

It is convenient to replace $S = s\alpha/R$ with $S/\cos\theta_i$, where $S_z = s\alpha/(z+h)$. S depends on the angle of incidence, while S_z depends only on the model and the wavelet, and depends unambiguously on a particular z. Our inputs therefore consist of 1) earth parameters, 2) angle of incidence, 3) n, s, α, and z, and 4) parameters controlling the numerical integration. The latter consists of two numbers, one to determine the grid width, and one to determine the upper cutoff for the second integral (which formally is $i \times \infty$). In the

calculations below we have chosen $|\Delta(\cos\theta)| = 0.001$ and $(\cos\theta)_{max} = 0.1i$. For plotting we have repeated the above calculation for incidence angles from 0° to 85° at 1° intervals. Neither decreasing the grid width nor increasing the cutoff produces any visible change to the plots. All of the calculations required for a plot can be performed in approximately 8.5 seconds of CPU time in MATLAB on a typical desktop PC. With a compiled code this time is somewhat less.

Results of calculation

We now present the result of calculations for this model. In Figure 2 we show spherical-wave results compared with plane wave results.

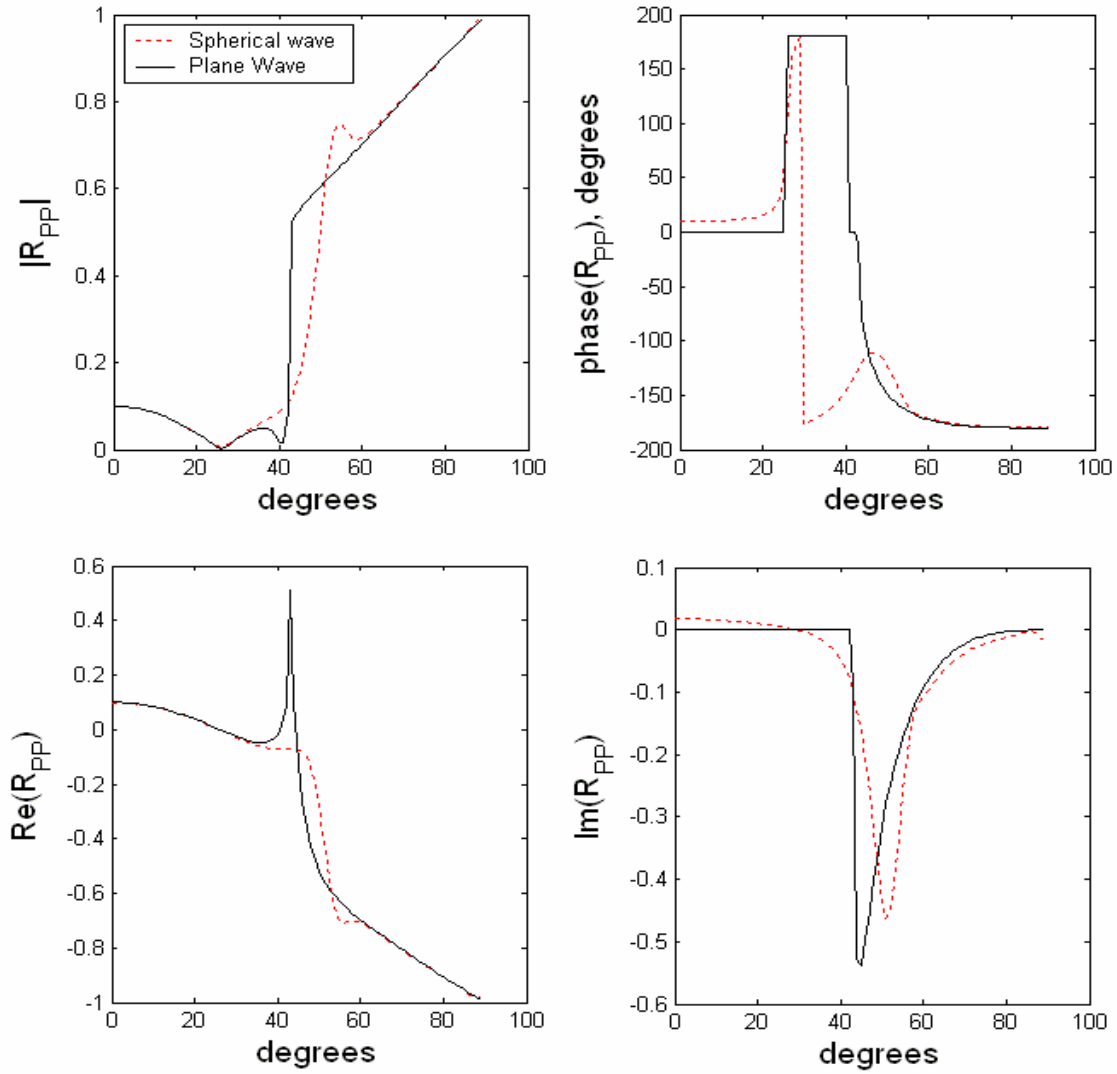

FIG. 2. Comparison of plane wave and spherical-wave reflection coefficients for the AVO Class I parameters of Table I. The wavelet is of the form of Eq. (3), with $n = 4$, $s = (.173\ \text{s})/(2\pi)$ [see Figure 1]. Note that significant spherical-wave effects are observed in the vicinity of the critical point.

It is clear that there are significant amplitude deviations in the region of the critical point, as noted by Haase (2004a). There are visible phase deviations at lower angles as well, but larger differences again near the critical point. In Figures 3a and 3b we compare the results of Figure 2 with calculation using the same wavelet, but by the method of Haase (2004a). We see excellent agreement throughout, although it is clear that the largest difference is just after the critical point. This likely arises from our assumptions regarding direction of propagation and arrival time. The smallness of even these differences though justifies the use of these assumptions for practical applications.

In Figure 3c we compare spherical-wave amplitudes for the two different wavelets shown in Figure 1. The exponential wavelet result in Figure 3 appears to give a stronger spherical effect than the Ormsby wavelet result. The Ormsby wavelet displays some oscillatory character just past the critical point. This is likely a Gibb's-type phenomenon related to the slope discontinuities in the Ormsby wavelet. Both wavelets yield a qualitatively similar deviation from the plane wave result, so that spherical effects are only mildly dependent on the precise shape of wavelet. Thus the specialized wavelets used in this study will be useful for at least qualitative investigation of spherical AVO effects.

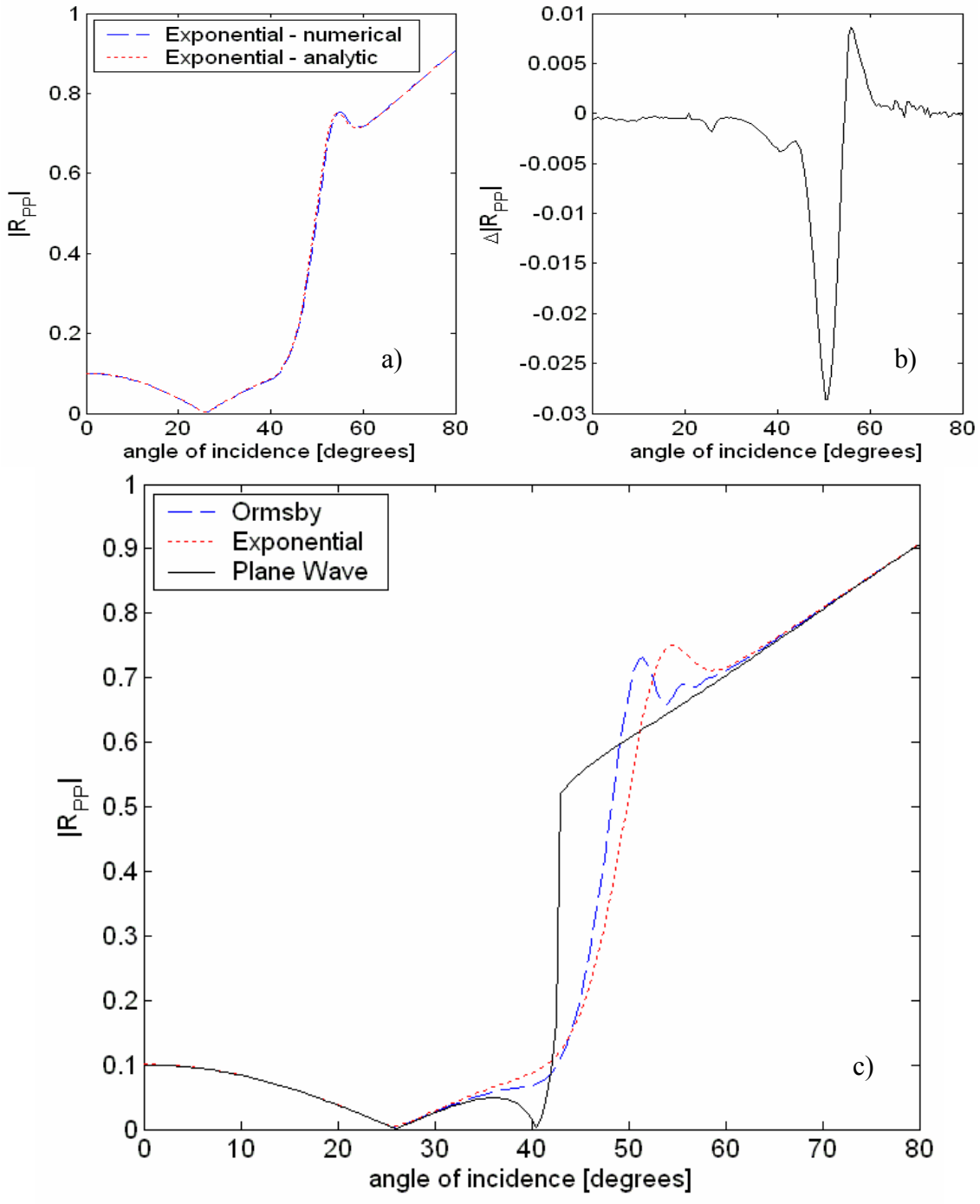

FIG. 3. Part a) shows a comparison of spherical-wave reflection coefficients calculated by both the present semi-analytic method and the fully numerical method of Haase (2004a). Both calculations employ the exponential wavelet of Figure 1. Part b) displays the difference of the two lines from part a). The largest difference occurs just after the critical point, which is at ~43°. Part c) compares spherical-wave reflection coefficients calculated for the two wavelets displayed in Figure 1. The Ormsby wavelet calculation uses the method of Haase (2004a) and the exponential wavelet calculation uses the present method. The plane-wave reflection coefficient is also included for comparison.

Implementation in a Java applet

Eq. (14) has also been implemented in a Java applet routine which may be executed interactively in a Java-enabled browser. A screen capture of the display for the same parameters used above is shown in Figure 4. In this software, changing the value of s, z, α_1, or n causes the program to recalculate W_n, which requires a few seconds. When changing other earth parameters however, a stored version of W_n is used, and the integration is rapid enough, that it can be recalculated and displayed several times a second, allowing for the effect of changing earth parameters to be investigated using a slider bar on the control panel. This is a useful tool for exploring the potential importance of spherical AVO effects for a given system of interest.

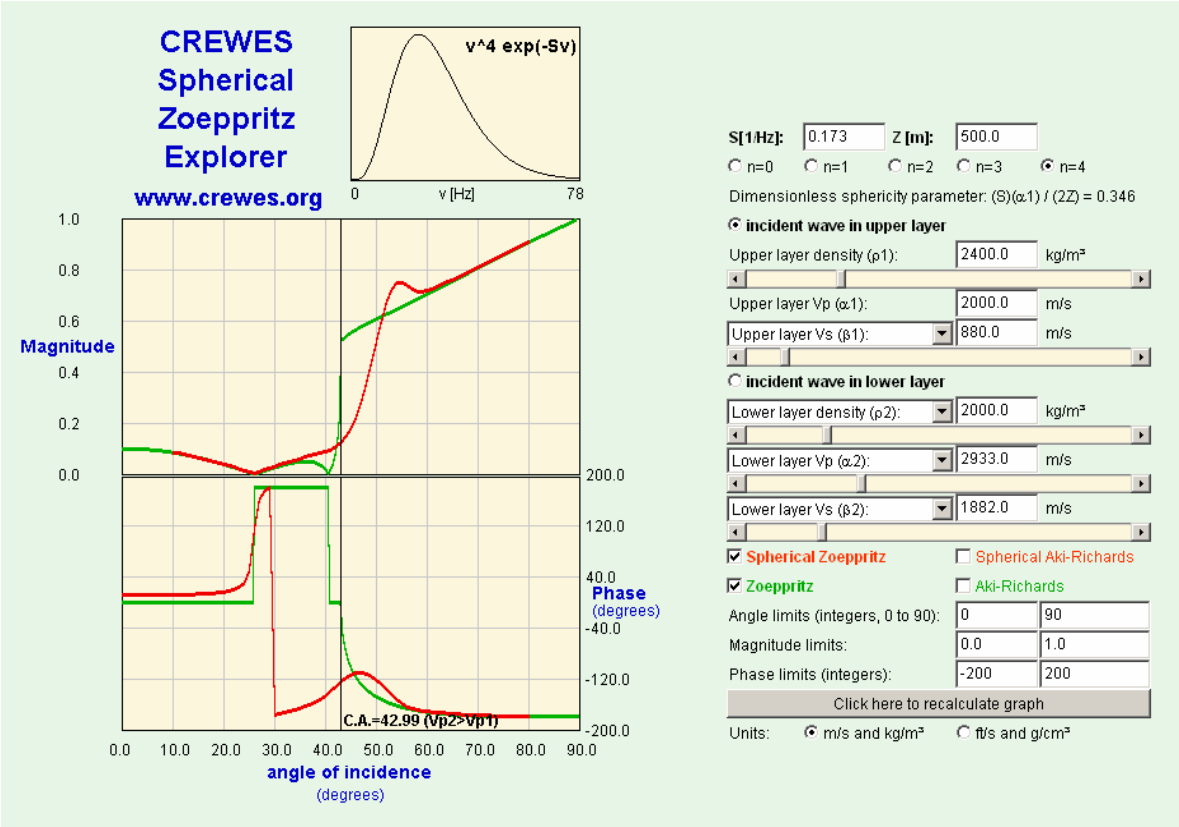

FIG. 4. Screen capture of the CREWES Spherical Zoeppritz Explorer, a Java applet implementation of Eq. (14). The parameters employed are the same as for Figure 2. Note that the parameter S in the control panel corresponds to $s/(2\pi)$ in the present study.

DISCUSSION

Haase (2004a) has also carried out calculations for a Class III AVO model and found that, in the absence of a critical point, the spherical-wave coefficients are very similar to the corresponding plane wave coefficients. To investigate this point, we display in Figure 5 some of the weighting functions, i.e.,

$$W_4(\theta; S_z, \theta_i) \equiv \left[\frac{i}{\alpha} \frac{\partial I}{\partial R} \div \left(-\frac{n!}{s^{n+1} R^2} + i \frac{(n+1)!}{\alpha s^{n+2} R} \right) \right]_{n=4}, \qquad (17)$$

which were employed in calculating the reflection coefficients of Figures 2 and 3. The weighting functions are displayed for particular values of θ_i, the angle of incidence. The weighting functions have both real and imaginary components. Integrating over the real components alone yields 1, and integrating over the imaginary components alone yields 0. Both components peak near the angle of incidence, and decay rapidly away from it. This explains why spherical effects are important near critical points. Away from the critical point, R_{PP} changes slowly, and can be viewed as roughly constant over the range of non-negligible weighting. Near the critical point however R_{PP} changes rapidly and the weighting function samples a considerable and non-linear range of values.

The nature of the weighting function has implications for practical calculations. It should be possible to carry out calculations more efficiently than has been done here, as it is only necessary to carry out numerical integrations within a compact range of the weighting function. In fact, the full spherical-wave coefficients are only necessary within a certain region of the critical point. Furthermore, the weighting functions are independent of all of the earth parameters (except the overburden P-wave velocity), so that in an AVO analysis it should only be necessary to calculate the weighting functions once in the course of an inversion. These and other measures may allow us to develop practical spherical-wave AVO inversion methods.

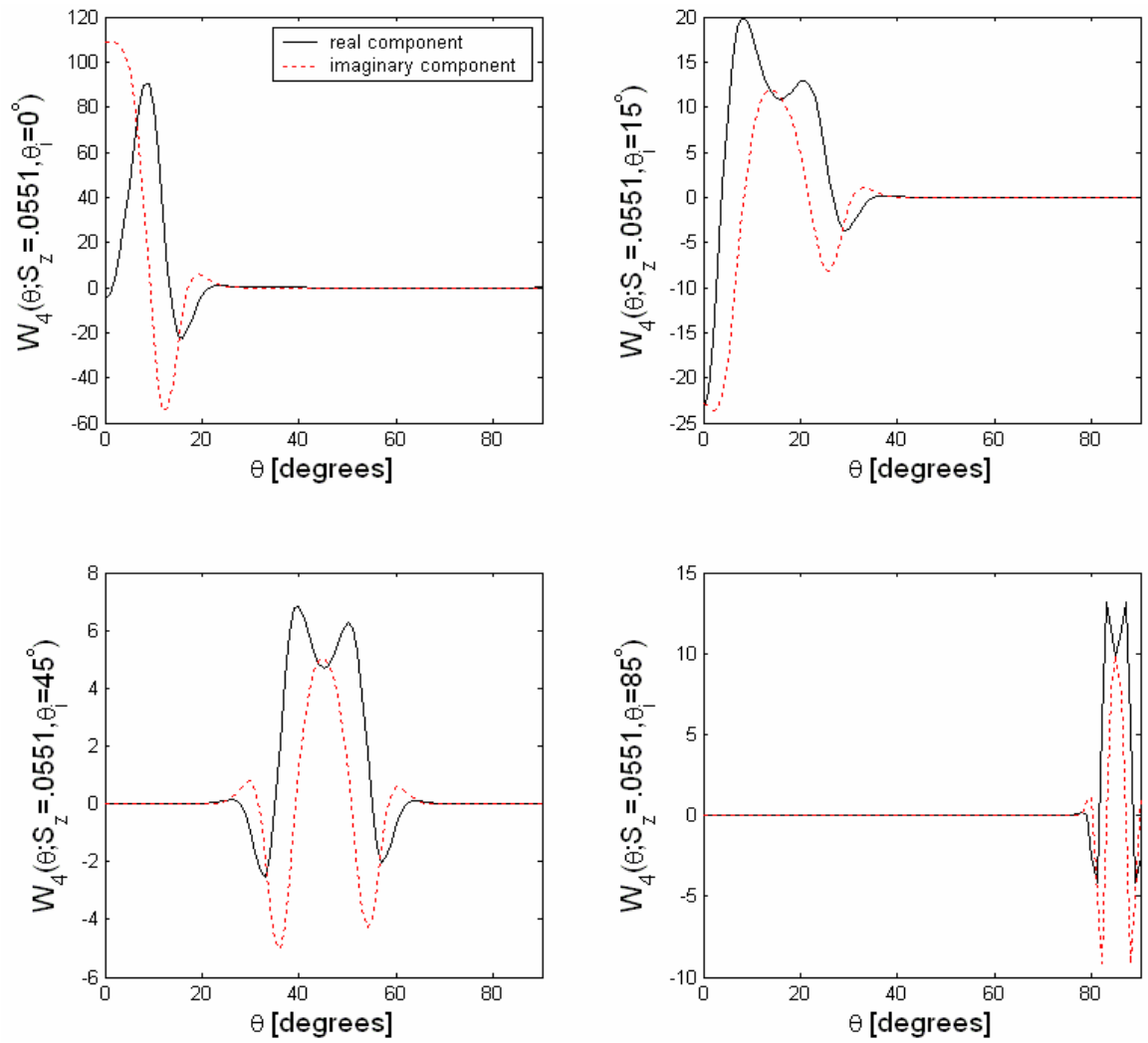

FIG. 5. Some of the weighting functions [i.e., Eq. (17)] used in calculating points in the plots of Figure 2. The weighting functions shown here are for incidence angles of a) 0°, b) 15°, c) 45°, and d) 85°. In each case both the real and imaginary components of the function are peaked near the angle of incidence.

In Figure 6 we have repeated the results of Figure 5, except that we have chosen a depth of 2000 m instead of 500 m. Spherical-wave effects are expected to decrease somewhat. In the weighting functions this translates into narrower peaks, which sample over a more restricted range of R_{PP}. For values of S or S_z decreasing to zero, the real component will approach a δ-function, as noted in the discussion following Eq. (16).

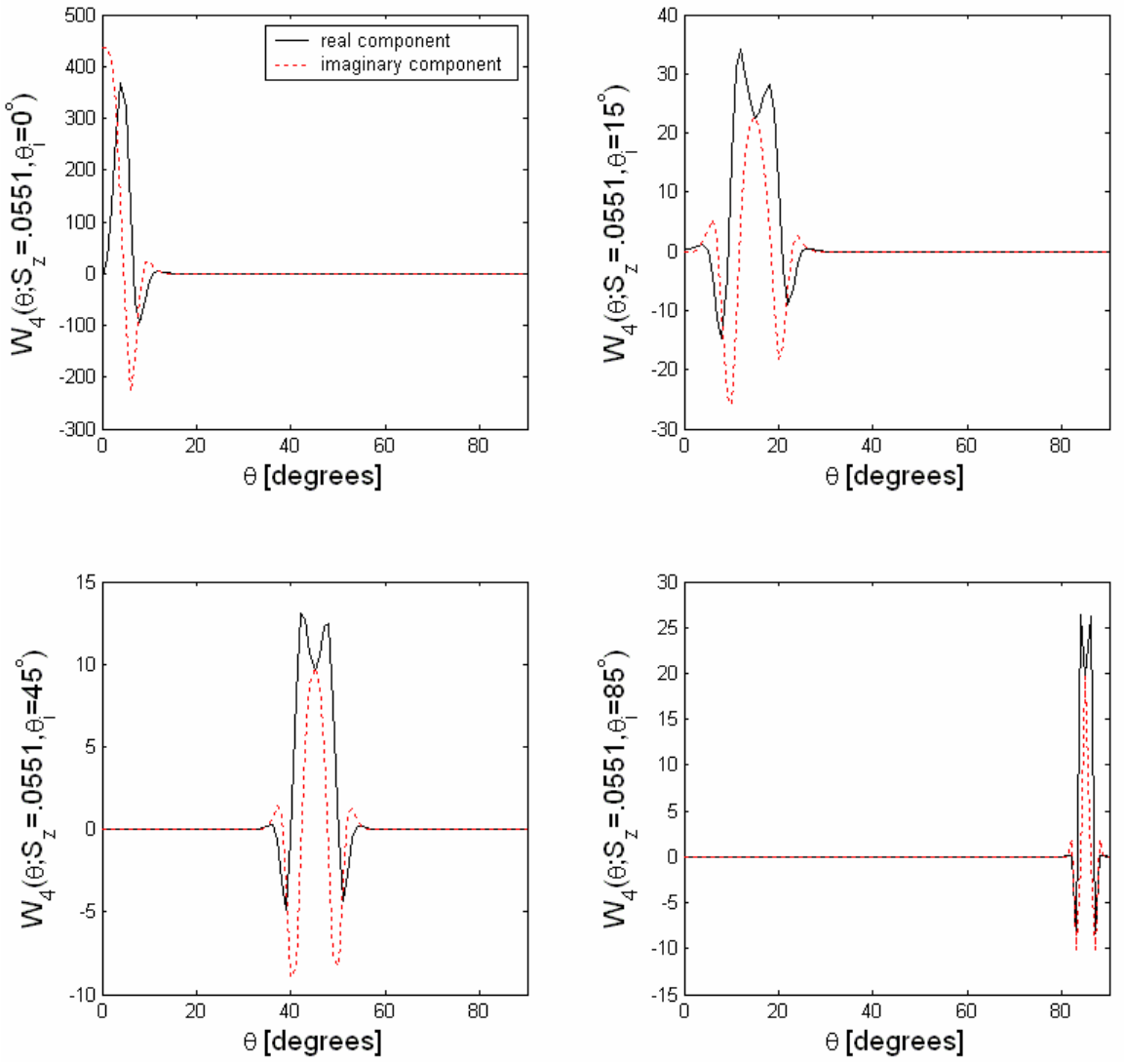

FIG. 6. This display is the same as Figure 5 but with $z = h = 2000$ m instead of $z = h = 500$ m. Comparing the two figures shows that as spherical effects decrease, the weighting functions become more sharply peaked.

We also observe in Figures 5 and 6 that spherical effects decrease with θ_i. This is reasonable, since the actual path length increases with θ_i at fixed depth, z. To investigate these matters more carefully, $|W_4|$ was calculated as a function of θ for several values of θ_i and S_z. The width of the peak was defined as the difference between two values of θ at which the function equals $1/100^{\text{th}}$ of the maximum peak height. The peak width is plotted in Figure 7a against θ_i, for three values of S_z. We have found that plotting against $S_z\cos\theta_i$ (= S) causes results for different S_z values to lie along the same line, and furthermore, plotting against $\sqrt{(S_z\cos\theta_i)}$ causes the plot to be roughly linear, as shown in Figure 7b.

This is of great practical value, as it provides a simple method for limiting the range of integration in Eq. (14) to a relatively small θ-interval.

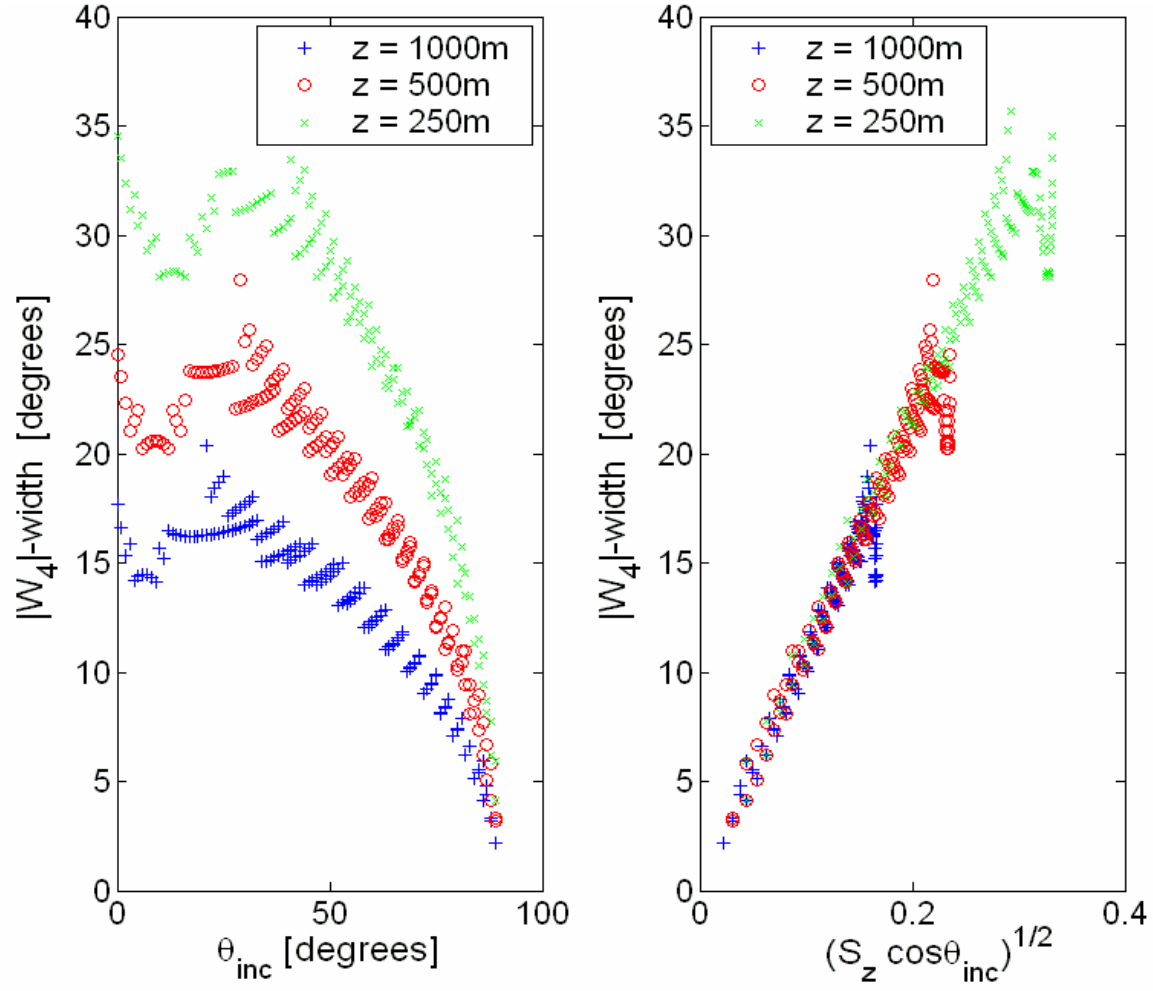

FIG. 7. The width of the peak of $W_4(\theta;\theta_i,S_z)$ when plotted as a function of θ, and its variation with θ_i and S_z [$=s\alpha/(z+h)$]. The width is shown to be linearly related to $(S_z\cos\theta_i)^{1/2}$. This is useful in reducing the range of numerical integrations in Eq. (14).

CONCLUSIONS

We have shown that, for a particular form of wavelet, one can reduce computation times for spherical-wave reflection coefficients. These show characteristics of behavior that are similar to more traditional wavelets. The efficiencies of this method also make it feasible to implement spherical-wave reflection coefficient calculations in an interactive Java applet. These calculations are nearly exact, with the main restriction being the form of the wavelet.

It has been shown how a spherical wave samples the plane wave reflection coefficients within a compact range around the angle of incidence. A quantitative description of this range may allow for even more efficient spherical-wave reflection coefficient

calculations in the future. Such developments considerably improve the prospects for practical spherical-wave AVO inversions.

REFERENCES

Aki, K. and Richards, P. G., 1980, Quantitative Seismology: Theory and Methods: W.H. Freeman, 1980.

Bortfeld, R., 1962, Reflection and Refraction of Spherical Compressional Waves at Arbitrary Plane Interfaces: Geophys. Prosp., **4**, 517-538.

Erdelyi, A., 1954, Tables of Integral Transforms, Vol. I, p. 182, New York, McGraw-Hill.

Furlong, J.R., Westbury, C.F., and Phillips, E.A., 1994, A method for predicting the reflection and refraction of spherical waves across a planar interface: J. Appl. Phys., **76**, 25-32.

Haase, A.B., 2002, Plane waves, spherical waves and angle-dependent P-wave reflectivity in elastic VTI-models, SEG Expanded Abstracts.

Haase, A.B., 2003, Approximation Errors in AVO-Analysis and Inversion, CSEG Expanded Abstracts.

Haase, A.B., 2004a, Spherical Wave AVO Modelling of Converted Waves in Elastic Isotropic Media, CSEG Expanded Abstracts. [See also Haase, A.B. and Ursenbach, C.P., 2004, Spherical wave AVO-modelling in elastic isotropic media, CREWES Research Report (this volume). This paper contains similar calculations to the CSEG abstract, but with the same normalization method as the present study.]

Haase, A.B., 2004b, Spherical Wave AVO Modeling of Converted Waves in Isotropic Media, SEG Expanded Abstracts.

Krail, P.M. and Brysk, J., 1983, Reflection of spherical seismic waves in elastic layered media: Geophys., **48**, 655-664.

Macdonald, C., Davis, P.M., and Jackson, D.D., 1987, Inversion of reflection traveltimes and amplitudes: Geophys., **52**, 606-617.

ACKNOWLEDGMENTS

The authors express appreciation Dr. E. Krebes for a careful reading of the manuscript and for several valuable suggestions.